Prediction of topological superconductivity from type-IV, -III, -II, and -I′ nodal points induced by Rashba spin-orbit coupling

Xiaoming Zhang [1,2,*] Da Gao [3] Xuhan Zhu,[1] Jiale Liu,[1] Wenshuang Wang,[2] Xiangdong Liu,[3] and Mingwen Zhao[3,†]

[1]*College of Physics and Optoelectronic Engineering, Ocean University of China, Qingdao, Shandong 266100, China*
[2]*National Glycoengineering Research Center, Shandong University, Qingdao, Shandong 266237, China*
[3]*School of Physics and State Key Laboratory of Crystal Materials, Shandong University, Jinan, Shandong 250100, China*

Topological superconductivity (TSC) has received great theoretical and experimental attention recently. Type-I Rashba nodal point (RNP) with isotropic band dispersions and point Fermi surface (FS) induced by the Rashba spin-orbit coupling (SOC) provides a promising route to the artificial TSC, because the inherent interspin coupling (ISC) shares identical form as the p-wave pairing ($k_x\sigma_y - k_y\sigma_x$) exactly. Here we discuss the potential TSC of other types of RNPs with different ISC forms. By constructing a generic tight-binding model with Rashba SOC, we demonstrate type-IV, -III, -II, and -I′ RNPs can be achieved on two-dimensional (2D) *Bravais* lattices, whose FS consists of only a hole (electron) pocket, two contacted hole (electron) pockets, contacted hole and electron pockets, and point of tangency, respectively. With the coorpration of s-wave pairing and Zeeman gaps, these new types of RNP will evoke TSC phases with chiral Majorana edge modes (MEMs), where the Chern number will be larger than 1 for multiple symmetry-equivalent RNPs. The Chern number can be further composited when the energies of unequivalent RNPs are equal, leading to edge-dependent MEMs. Moreover, by using first-principles calculations, we demonstrate the BiSb monolayer is an ideal platform for realizing TSC with Chern number 6 from type-II, -I, or -IV RNP. This work enriches the types of nodal point induced by Rashba SOC and offers a generic guidance on realizing multiple and edge-dependent MEMs from the abundantly synthesized 2D surface metal layers.

I. INTRODUCTION

Topological superconductivity (TSC) represents a nontrivial phase of condensed-matter systems characterized by the gapless/zero-energy Majorana boundary modes within the bulk superconducting gap [1–3], which have received extensive research interest in recent years due to the pivotal utilization of fault-tolerant topological quantum computation [4–7]. In addition to intrinsic TSC with p-wave pairing gap [8,9], artificial chiral TSC has won great experimental achievements [10–13], stimulated by the extensively theoretical proposals of realizing effective p-wave gap from the combination of Rashba spin-orbital coupling (SOC), s-wave superconductivity (SC), and time-reversal symmetry breaking [14–18]. The underlying mechanism can be understood by that the employed nodal point induced by Rashba SOC possesses the type-I features of isotropic linear band dispersions and point Fermi surface (FS) [19], named as type-I Rashba nodal point (RNP), where the interspin coupling (ISC) shares identical form as the p-wave pairing ($k_x\sigma_y - k_y\sigma_x$) exactly. This physical picture is applicable to explain the TSC of topological surface states with similar isotropic nodal point [20–26]. Considering the type-I Weyl nodal point described by $\pm(k_x\sigma_x + k_y\sigma_y + k_z\sigma_z)$ possesses type-II and -III

counterparts [19,27,28], it is necessary to explore the possibility of other type RNPs with different low-energy effective ISC, as well as their feasibility of hosting TSC phases.

Topological invariant is widely used to characterize the specific phases of TSC and their difference [29]. For two-dimensional (2D) chiral TSC phase, the topological invariant is Chern number C, which usually describes the number of one-dimensional (1D) chiral Majorana edge modes (MEMs) on each edge that propagate along the same direction. The propagation could enable the half-quantized charge conductance [21,22,30], the half-integer thermal Hall conductance [31,32], as well as the same unitary transformation as braiding Majorana zero modes [33,34]. It is of practical importance to find high Chern numbers TSC phases associated with multiple MEMs, in order to enhance these exotic transport properties and promote the critical applications in related fields. Meanwhile, exploring the possibility of realizing MEMs that cannot be solely determined by the Chern number but also depend on edge directions will be of fundamental significance for tuning MEMs within one TSC phase.

By now, theoretical works propose that s-, p-, and d-wave SC all can give rise to high Chern number TSC phases under certain conditions [21,35–39]. Especially for the artificial chiral TSC with s-wave pairing [40–44], the high Chern number was confirmed in the van der Waals heterostructures combining 2D ferromagnet and superconductor [13]. However, these achievements are limited on the lattice structures with high symmetry, where the type-I RNPs at time-reversal invariant
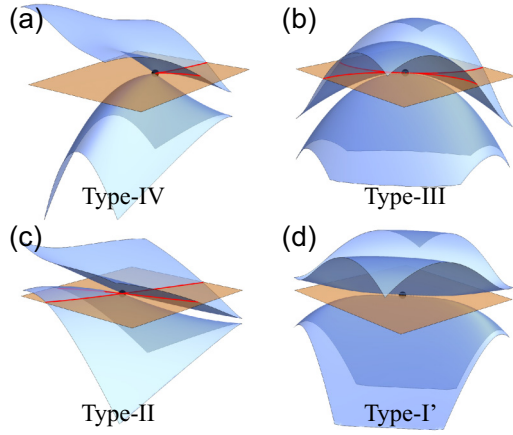
*zxm@ouc.edu.cn
†zmw@sdu.edu.cn

FIG. 1. The schematic diagrams of (a) type-IV, (b) type-III, (c) type-II, and (d) type-I′ RNPs. The red lines represent the FS contours plotted by assuming the Fermi level (orange plane) locating at the energy of nodal point (black dot).

(TRI) points are responsible for the nontrivial phases. Consequently, one natural question is the robustness of the TSC when the lattice symmetry is lowered and/or the RNPs are deviated from the TRI point. Together with the abundant 2D metal layers with diversiform lattice structures fabricated on substrate materials [45–56], it is urgently needed to investigate the potential TSC phases of all the *Bravais* lattices within 2D crystal system (2DCS). This extension will be beneficial to search more TSC candidates from the ultrathin films grown on substrates [57], where the desired Rashba SOC stems from the inherent space-inversion asymmetry and the *s*-wave SC can be intrinsic [48,50–52] or induced by proximity.

In this paper, we demonstrate a number of RNPs (type IV, III, II, and I′) with the low-energy effective ISC different from $(k_x\sigma_y - k_y\sigma_x)$ by constructing a generic tight-binding (TB) model with Rashba SOC effect on 2D *Bravais* lattices. Type-IV RNP represents a new type of nodal point since its FS only consists of a hole (electron) pocket [Fig. 1(a)]. This type of nodal point was not reported even in the field of the extensively studied Weyl nodal points. Type-III RNP is similar to the recently proposed type-III Weyl nodal point [27,28], whose FS possesses two contacted hole (electron) pockets [Fig. 1(b)]. The FS of type-II RNP is constructed by contacted hole and electron pockets [Fig. 1(c)], similar to that of type-II Weyl nodal points [19]. Type-I′ RNP is analogous to the type-I one when regarding the point FS. We use the "prime" to distinguish them because the type-I′ RNP is enabled by the spin-splitted bands with high-order dependence on momentum vector **k** [Fig. 1(d)]. Type-III and type-I′ RNPs at TRI point are the degenerated point enforced by Kramers theorem, while type-IV and -II ones are different and will emerge at the **k** points deviated from the TRI point. These RNPs will provide promising platforms to investigate physics of Rashba SOC.

With the cooperation of *s*-wave pairing and Zeeman gaps, all these RNPs are demonstrated to enable the artificial TSC phases with nonzero Chern number. Multiple MEMs can be realized for multiple symmetry-equivalent RNPs, where the RNPs deviated from the TRI point present advantages over
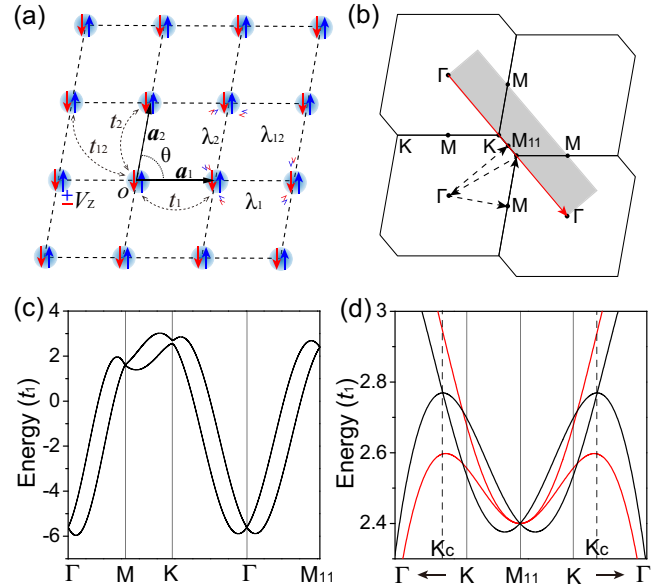

FIG. 2. (a), (b) The schematic diagrams of (a) generic TB model on 2DCS and (b) the corresponding TRI points in its BZ. (c), (d) The examples of band structure along the high-symmetry directions marked by (c) the black dashed lines and (d) the red solid line in (b). The values of $t_1 = 1.0$, $t_{12} = 0.8t_1$, $\lambda_1 = 0.5t_1$, and $\lambda_{12} = 0.41t_1$ are used for calculating the bands plotted by black color in (c) and (d), while the red one in (d) is calculated by changing the λ_{12} to $0.32t_1$.

the ones at the TRI point in inducing the high Chern number phases. Meanwhile, the Chern number could be further composited when the unequivalent RNPs are equal in energy, which provides the opportunity of tuning the number of chiral MEMs by changing edge directions within one TSC phase. Furthermore, by using first-principles calculations, we demonstrate BiSb monolayer with honeycomb lattice is an ideal material platform for realizing the type-I, type-II, and even type-IV RNPs at the **k** point deviated from the TRI point, which can induce TSC phase with Chern number $C = 6$. Fabricating the BiSb on substrate will give rise to the type-III RNP at the TRI point. We emphasize that our proposed types of RNP widely exist in 2D materials with the inversion symmetry being broken by buckling or substrates, whose TSC phases will greatly expand the horizon of finding multiple and edge-dependent MEMs.

II. GENERIC TB MODEL OF 2DCS

The real-space TB model of 2DCS with electron hopping h_t, the Rashba SOC h_R, and the out-of-plane directed Zeeman exchange field h_Z can be generally written as

$$H = h_t + h_R + h_Z, \qquad (1)$$

$$h_t = -t_{NN} \sum_{\langle m,n \rangle, \alpha} c_{m,\alpha}^\dagger c_{n,\alpha}, \qquad (2)$$

$$h_R = i\lambda_{NN} \sum_{\langle m,n \rangle, \alpha \neq \beta} (\boldsymbol{\sigma}^{\alpha\beta} \times \mathbf{d}_{mn}) \mathbf{e}_z c_{m\alpha}^\dagger c_{n\beta}, \qquad (3)$$

$$h_Z = V_Z \sum_{m,\alpha} c_{m\alpha}^\dagger \sigma_z c_{m\alpha}. \qquad (4)$$

Here $\langle m, n \rangle$ represents the nearest-neighboring (NN) sites, and $c_{m,\alpha}$ ($c_{m,\alpha}^{\dagger}$) annihilates (creates) the electron with spin α at m site. Each lattice site possesses a single orbital that includes up- and down-spin components. $t_{\rm NN}$ ($\lambda_{\rm NN}$) denotes the magnitude of hopping energy (Rashba SOC strength) between NN sites along the line being parallel with the lattice vector $\boldsymbol{a}_1$, $\boldsymbol{a}_2$, and $\boldsymbol{a}_1 - \boldsymbol{a}_2$ (or $\boldsymbol{a}_2 - \boldsymbol{a}_1$), which are marked as t_1 (λ_1), t_2 (λ_2), and t_{12} (λ_{12}) [see Fig. 2(a)], respectively. $\boldsymbol{d}_{mn}$ is the unit vector pointing from site n to m and $\boldsymbol{e}_z$ is the unit vector along the z direction. $\boldsymbol{\sigma} = (\sigma_x, \sigma_y, \sigma_z)$ is the Pauli vector for spin and Vz represents the magnitude of Zeeman energy.

We introduce the parameter of angle θ between the $\boldsymbol{a}_1$ and $\boldsymbol{a}_2$ [Fig. 2(a)], to enable the generic discussion for 2DCS. Specifically, if $|\boldsymbol{a}_1| = |\boldsymbol{a}_2|$, $\theta = 90°$ and $60°$, respectively, represents the square and hexagonal *Bravais* lattices, while the other degree corresponds to the centered rectangular lattice, as shown by Fig. S1 in the Supplemental Material (SM) [58]. Similarly, $|\boldsymbol{a}_1| \neq |\boldsymbol{a}_2|$ gives rise to the rectangular lattice when $\theta = 90°$ [Fig. S2(a)], while the oblique lattice will be formed when $\theta \neq 90°$ [Fig. S2(b)]. Without loss of generality, we take $\theta = 80°$ as the example to perform numerical calculations in this paper. Under the basis of $\phi_{\bf k} = (c_{{\bf k}\uparrow}, c_{{\bf k}\downarrow})^{\rm T}$, the real-space Hamiltonian of Eq. (1) can be written into momentum space:

$$H = \sum_{\bf k} \phi_{\bf k}^{\dagger} h(k_x, k_y) \phi_{\bf k}, \tag{5}$$

$$h(k_x, k_y) = \begin{pmatrix} h_t(k_x, k_y) + V_Z & h_R(k_x, k_y) \\ h_R^*(k_x, k_y) & h_t(k_x, k_y) - V_Z \end{pmatrix}. \tag{6}$$

It is unambiguous that the electrons with different spin are interacted by the Rashba SOC, which acts as the so-called ISC.

Then, the Bogoliubov–de Gennes (BdG) Hamiltonian with the s-wave pairing $\Delta_s = i\Delta\sigma_y$ condensing at the chemical protential μ was constructed under the basis of $\varphi_{\bf k} = (c_{{\bf k}\uparrow}, c_{{\bf k}\downarrow}, c_{-{\bf k}\uparrow}^{\dagger}, c_{-{\bf k}\downarrow}^{\dagger})^{\rm T}$:

$$H_{\rm BdG} = \frac{1}{2}\sum_{\bf k} \varphi_{\bf k}^{\dagger} h_{\rm BdG}(k_x, k_y) \varphi_{\bf k}, \tag{7}$$

$$h_{\rm BdG}(k_x, k_y) = \begin{pmatrix} h(k_x, k_y) - \mu & \Delta_s \\ \Delta_s^* & -h^*(-k_x, -k_y) + \mu \end{pmatrix}. \tag{8}$$

This BdG Hamiltonian enables one to discuss the artificial TSC phases of RNPs by calculating the Chern number C. The chiral MEMs of TSC phases could be obtained by extending the BdG Hamiltonian to that of 1D nanoribbon with two opened edges.

III. PROPOSAL OF TYPE-IV, TYPE-III, TYPE-II, AND TYPE-I′ RNPS

We first discuss RNPs on 2D square, hexagonal, and centered rectangular *Bravais* lattices by assuming $\boldsymbol{a}_1 = (1, 0)$ and $\boldsymbol{a}_2 = (\cos\theta, \sin\theta)$ [Fig. 2(a)], which results in $t_1 = t_2$ and $\lambda_1 = \lambda_2$ in the TB model. The matrix elements of the momentum space Hamiltonian Eq. (6) can be written as

$$h_t(k_x, k_y) = -2t_1[\cos k_x + \cos(k_x \cos\theta + k_y \sin\theta)] - 2t_{12}\cos[k_x(1 - \cos\theta) - k_y \sin\theta], \tag{9}$$

$$h_R(k_x, k_y) = -2i\lambda_1[\sin k_x + (\cos\theta - i\sin\theta)\sin(k_x \cos\theta + k_y \sin\theta)]$$
$$+ \sqrt{\frac{2}{1 - \cos\theta}}\lambda_{12}[i(\cos\theta - 1) + \sin\theta]\sin(k_x - k_x \cos\theta - k_y \sin\theta). \tag{10}$$

The eigenvalues at the TRI points of the Brillouin zone (BZ) [Fig. 2(b)] are then obtained by diagonalizing the constructed Hamiltonian:

$$E(\boldsymbol{\Gamma}) = -4t_1 - 2t_{12} \pm V_Z, \tag{11}$$

$$E(\boldsymbol{M}) = 2t_{12} \pm V_Z, \tag{12}$$

$$E(\boldsymbol{M}_{11}) = 4t_1 - 2t_{12} \pm V_Z, \tag{13}$$

$$E(\boldsymbol{K}) = 2t_1\left[\cos\left(\frac{\pi\cos\theta}{1 + \cos\theta}\right) - \cos\left(\frac{\pi}{1 + \cos\theta}\right)\right] + 2t_{12}\cos\left(\pi\tan\left(\frac{\theta}{2}\right)^2\right) \pm \sqrt{A + V_Z^2}, \tag{14}$$

where $A = -2\lambda_1^2 A_1 + 4\lambda_{12}^2 A_{12} - 4\lambda_1\lambda_{12}A_{112}$, with

$$A_1 = -2 + \cos(\pi\sec^2(\theta/2)) + \cos(\pi\cos\theta\sec^2(\theta/2)) + 2\cos\theta[1 + \cos(\pi\tan^2(\theta/2))], \tag{15}$$

$$A_{12} = \sin^2(\pi\tan^2(\theta/2)), \tag{16}$$

$$A_{112} = \sqrt{2 - 2\cos\theta}\left[\sin\frac{\pi}{1 + \cos\theta} + \sin\frac{\pi\cos\theta}{1 + \cos\theta}\right]\sin\left(\pi\tan^2\frac{\theta}{2}\right). \tag{17}$$

One can easily identify a Zeeman gap of $2V_Z$ opened at these TRI points except the K point. The Zeeman gap of $2\sqrt{A + V_Z^2}$ at the K point is not only dependent on the magnitude of Zeeman energy, but also determined by the effective "Zeeman field" of $\sqrt{A}$ that is related to the Rashba SOC strength and the angle θ. This means that even if $V_Z = 0$, a gap could still persist if $A \neq 0$ at the K point, contrary to the formation of type-I RNPs at other TRI points [Fig. 2(c)]. The $A = 0$ at the K point can be fulfilled for square lattice [$\theta = 90°$ and assuming $t_{12} = \lambda_{12} = 0$; see Fig. S1(a)] and hexagonal lattice [$\theta = 60°$ and assuming $\lambda_1 = \lambda_{12}$; see Fig. S1(b)], where the M_{11} is evolved into the K [Fig. S1(d)] and M [Fig. S1(e)] point, respectively. For the centered rectangular *Bravais* lattices [Fig. S1(c)], the $A = 0$ will emerge at the K_c point with the following coordinate and eigenvalue when $V_Z = 0$:

$$K_c = \left(\pm \operatorname{Arccos}\left(-\frac{\lambda_1\sqrt{1 - \cos\theta}}{\sqrt{2}\lambda_{12}} \right), \right.$$
$$\left. \mp \operatorname{Arccos}\left(-\frac{\lambda_1\sqrt{1 - \cos\theta}}{\sqrt{2}\lambda_{12}} \right)\frac{1 + \cos\theta}{\sin\theta} + \frac{2\pi}{\sin\theta} \right), \quad (18)$$

$$E(K_c) = \frac{2\sqrt{2}t_1\lambda_1\lambda_{12}\sqrt{1 - \cos\theta} + 2t_{12}\left[\lambda_{12}^2 - \lambda_1^2(1 - \cos\theta)\right]}{\lambda_{12}^2}. \quad (19)$$

We emphasize that the K_c is different from the TRI K point if $\lambda_1\sqrt{1 - \cos\theta} + \sqrt{2}\lambda_{12}\cos[\pi/(1 + \cos\theta)] \neq 0$. One example of the band structure is plotted by the black line in Fig. 2(d), where the type-IV RNP comes into being at the K_c point. The type-IV RNP can transform into type-I and -II RNPs under different parameters, and will be eliminated when $\eta = \lambda_1^2(1 - \cos\theta) - 2\lambda_{12}^2 \geqslant 0$. For $\eta = 0$, type-III (or type I′, see below) RNPs will be formed at the M_{11} point [red line in Fig. 2(d)], where the related two bands present high-order dependence on the momentum vector **k**.

To show the evolution between these different types of RNP more clearly, we calculate the eigenvalues at the **k** points within the 2D shaded region [Fig. 2(b)], as shown by Fig. S3 in the SM [58]. One can see the type-I RNP [Fig. S1(a)] will evolve into type-III RNP [Fig. S3(b)] at the M_{11} point with the increase of λ_{12}. Then, the type-II [Fig. S3(c)], type-IV [Fig. S3(d)], and type-I [Fig. S3(e)] RNPs emerge sequentially at the K_c point when further increasing the λ_{12}. Additionally, $t_1 = 2t_{12}$ will transform the type-III RNP to type-I′ RNP at the M_{11} point [Fig. S3(f)]. The FS of these RNPs are plotted in Fig. S4 [58], which clearly shows only a hole pocket [Fig. S4(a)], two contacted hole pockets [Fig. S4(b)], contacted electron and hole pockets [Fig. S4(c)], and point of tangency [Fig. S4(d)] for the type-IV, type-III, type-II, and type-I′ RNPs, respectively.

For rectangular and oblique *Bravais* lattice, the $|\boldsymbol{a}_1| \neq |\boldsymbol{a}_2|$ will lead to $t_1 \neq t_2$ and $\lambda_1 \neq \lambda_2$ [Fig. 2(a) and Fig. S2] [58]. By assuming $|\boldsymbol{a}_2| = |l\boldsymbol{a}_1|$ ($l \neq 1, 0$), the matrix elements of $h(k_x, k_y)$ [Eq. (6)] should be rewritten as

$$h_t(k_x, k_y) = -2t_1\cos k_x - 2t_2[\cos(k_x l\cos\theta + k_y l\sin\theta)]$$
$$- 2t_{12}\cos[k_x(1 - l\cos\theta) - k_y l\sin\theta], \quad (20)$$

$$h_R(k_x, k_y) = -2i\lambda_1\sin k_x - 2i\lambda_2[(\cos\theta - i\sin\theta)$$
$$\times \sin(k_x l\cos\theta + k_y l\sin\theta)]$$
$$+ 2\lambda_{12}[i(l\cos\theta - 1) + l\sin\theta]$$
$$\times \sin(k_x - k_x l\cos\theta - k_y l\sin\theta)$$
$$/\sqrt{1 + l^2 - 2l\cos\theta}. \quad (21)$$

There are one $\boldsymbol{\Gamma}$, one M_{10}, one M_{01}, one M_{11}, and two K TRI points in the first BZ (Fig. S2(d) [58]). For the former four TRI points, type-I RNPs emerge at the energies of $E(\boldsymbol{\Gamma}) = -2(t_1 + t_2 + t_{12})$, $E(M_{10}) = 2(t_1 - t_2 + t_{12})$, $E(M_{01}) = 2(-t_1 + t_2 + t_{12})$, and $E(M_{11}) = 2(t_1 + t_2 - t_{12})$, which definitely enable the formation of TSC phase. Meanwhile, type-IV [Fig. S5(a)], type-II [Fig. S5(b)], and type-I [Fig. S5(c)] RNPs at the **k** points deviated from the TRI point can be induced under specific parameters, which is similar to the above case of $|\boldsymbol{a}_1| = |\boldsymbol{a}_2|$. Consequently, without losing generality, we take $|\boldsymbol{a}_1| = |\boldsymbol{a}_2|$ as the example to discuss the potential TSC phase of the newly proposed RNPs in the following section.

IV. TSC PHASES OF THE PROPOSED RNPS

As one of the most promising routes to the artificial TSC, type-I RNP has been discussed extensively [14–18], which will evoke the TSC phase when $V_Z^2 > \Delta^2 + (E_{\text{RNPs}} - \mu)^2$ (E_{RNPs} is the energy where the RNP is locating). We will mainly focus on potential TSC of the newly proposed type-IV, -III, -II, and -I′ RNPs (Fig. 1) when both s-wave pairing and Zeeman gaps are introduced. For simplify, we assume $\mu = E_{\text{RNPs}}$ for the considered RNP and employ the values of V_Z and Δ that always fulfill the condition of $V_Z^2 > \Delta^2$.

The BdG Hamiltonian of SC is constructed based on Eq. (8) for the considered RNPs, which enable us to calculate the superconducting quasiparticle band dispersions by diagonalization (Fig. 3). It is obvious that the pairing gaps are fully opened around the zero energy, where the electron and hole branch bands mix with each other (green colored bands in Fig. 3). However, the gaps show the feature of multiple magnitudes, different from the same sized pairing gap of type-I RNP. For type-IV RNP, a gap minimum emerges near the K point [Fig. 3(a)], while the minimum locates at the M_{11}-K path for type-III RNP [Fig. 3(b)]. Type-II RNP possesses gap minima on either side of the K point [Fig. 3(c)]. We argue the decreased gap magnitudes stem from the suppression of Pauli paramagnetic mechanism, when comparing the distributions of spin polarizations for the electronic states on the FSs (Fig. S6 [58]). One can easily identify the gap minima emerge at the **k** point where the electron states possess large out-of-plane spin polarization, which are parallel at **k** and **-k** points. This feature is known to be detrimental to the s-wave SC and thus suppresses the magnitudes of pairing gap. Differently, the expectation values of σ_z are nearly zero on the FS of type-I′ RNP [Fig. S6(d)], which lead to the pairing gap being nearly identical [Fig. 3(d)], similar to the type-I RNP.

Despite with different magnitudes, the fully opened gap ensures a well-defined Chern number C. We calculated the Berry curvature of all the quasiparticle states below the pairing
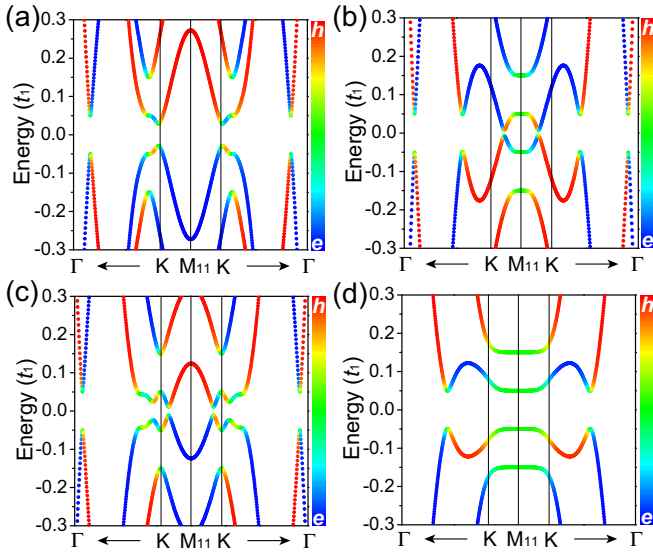
FIG. 3. The superconducting quasiparticle band dispersions of (a) type-IV, (b) type-III, (c) type-II, and (d) type-I′ RNP. In (a)–(c), the values of $t_1 = 1.0$, $t_{12} = 0.8t_1$, and $\lambda_1 = 0.5t_1$ are identical in the TB model, and the value of λ_{12} is (a) $0.41t_1$, (b) $0.32t_1$, and (c) $0.36t_1$. The values of $t_1 = 1.0$, $t_{12} = 0.5t_1$, $\lambda_1 = 0.5t_1$, and $\lambda_{12} = 0.32t_1$ are used in (d). $\Delta = 0.05t_1$ and $V_Z = 0.1t_1$ are employed to construct the BdG Hamiltonian, Eq. (8). The blue (red) color represents the component of electron (hole) branches.

gap (Fig. S7 [58]), which shows nonzero Berry curvature distributes around the FS contours and is especially pronounced at the **k** points with large out-of-plane spin polarization (Fig. S6 [58]). Integrating the Berry curvature over the first BZ leads to the Chern number of $C = 2$ for the type-IV and type-II RNP at the K_c point, while the $C = -1$ is evaluated for the type-III and type-I′ one at the M_{11} point (Table I). To further demonstrate the topological nontriviality, we calculated the quasiparticle band dispersions of 1D nanoribbons with the periodic direction along a_1 (Fig. S8 [58]), i.e., (100) direction. One can clearly see the existence of chiral MEMs within the superconducting gap, and the number of the MEMs residing at each edge is equal to the Chern number C. This indicates these RNPs indeed spark nontrivial TSC phases. Interestingly, except the type-I′ RNP [Fig. S8(d)], a significant feature different from the type-I RNP is the existence of bulk

TABLE I. The Chern number C of the RNPs at symmetry-equivalent **k** points for the centered rectangular, square, and hexagonal *Bravais* lattices. The labels of TRI points are marked in Fig. S1.

TRI Points	Γ	K_c	M_{11}	M	Notes
Centered rectangular lattice	1	2	−1	−2	$\eta < 0$
	1	–	1	−2	$\eta \geqslant 0$
Square lattice	1	–	1	−2	M_{11} becomes K
Hexagonal lattice	1	2	–	−3	M_{11} becomes M; K_c becomes K

states within the superconducting gap [Figs. S8(a)–S8(c)]. This is also attributed to the Pauli paramagnetic mechanism suppressing the magnitude of superconducting gap (Fig. 3). If the suppressing effect is large enough to closing the superconducting gap at certain **k** points when the Zeeman (pairing) gap is increased (decreased), nodal TSC phase with the Majorana zero-energy edge modes are expected to emerge [59].

We emphasize that the value of Chern number is fundamentally rooted in the number of symmetry-equivalent **k** points associated with the RNP in the first BZ. This is further confirmed by the calculated Chern number (Table I) for the type-I RNPs at the symmetry-enforced one Γ, two equivalent M, and one M_{11} points [Fig. 2(b)]. The Chern number at specific TRI point of the centered rectangular lattices is similar to that of square lattice (hexagonal lattice) for $\eta \geqslant 0$ ($\eta < 0$), when considering the corresponding relations between the TRI points of different *Bravais* lattices [Figs. S1(d)–S1(f)] [58]. Notably, the Chern number can be enlarged in the lattice with higher symmetry. For example, $E(M) = E(M_{11})$ can be easily realized in the hexagonal lattice with $t_1 = t_{12}$ and $\lambda_1 = \lambda_{12}$, which will lead to the Chern number of -3 that is evaluated by summing the Chern number at M and M_{11} points (Table I).

In addition to the symmetry-enforced high Chern numbers C, the RNPs at unequivalent **k** points could be equal in energy under specific parameter values in the generic TB model, which provides opportunities to composite the Chern number and MEMs. For example, the $E(K_c)$ and $E(M_{11})$ will be equal with each other when $t_1(2\lambda_{12}^2 - \lambda_1\lambda_{12}\sqrt{2 - 2\cos\theta}) = t_{12}[2\lambda_{12}^2 - \lambda_1^2(1 - \cos\theta)]$. The summation of Chern number associated with the RNPs at K_c and M_{11} points (Table I) generates the composited Chern number of 1. However, by constructing 1D nanoribbon along the (100) direction, the MEMs are calculated to be three residing on each edge [Fig. 4(a)], unequal to the composited Chern number. On the contrary, the number of MEMs on the edge of 1D ribbon with the periodic direction of $a_1 + a_2$ [Fig. 4(b)], i.e., (110) direction, is equal to the composited Chern number [Fig. 4(b)]. This indicates the number of MEMs depends on the edge directions, which will provide promising opportunity of tuning the MEMs within one composited TSC phase.

To understand this interesting behaver, we analyze the MEMs of $C = -1$ (or 2) TSC phase solely induced by the RNPs at M_{11} (or K_c) point when $E(K_c) \neq E(M_{11})$ (Fig. S9 [58]). The $C = -1$ phase give rise to one MEM near the momentum π on each edge of the (100) ribbon [Fig. S9(a)], while the two MEMs of $C = 2$ phase deviate from the high-symmetry points of the BZ [Fig. S9(b)]. This separation in momentum space ensures the MEMs with opposite chirality being not canceled out even at the same edge, which induce three MEMs [Fig. 4(a)] when the two TSC phases are composited. Actually, the position of MEMs in 1D BZ is closely related to the projected points of RNPs. Because both the RNPs at K_c and M_{11} points will be projected to the same **k** point in the BZ of (110) ribbon, the MEMs of associated TSC phases cannot be separated from each other in momentum space [Figs. S9(c) and S9(d)]. Then, the MEMs with opposite chirality will annihilate each other, leading to the consistence between composited Chern number and the number of MEMs [Fig. 4(b)].
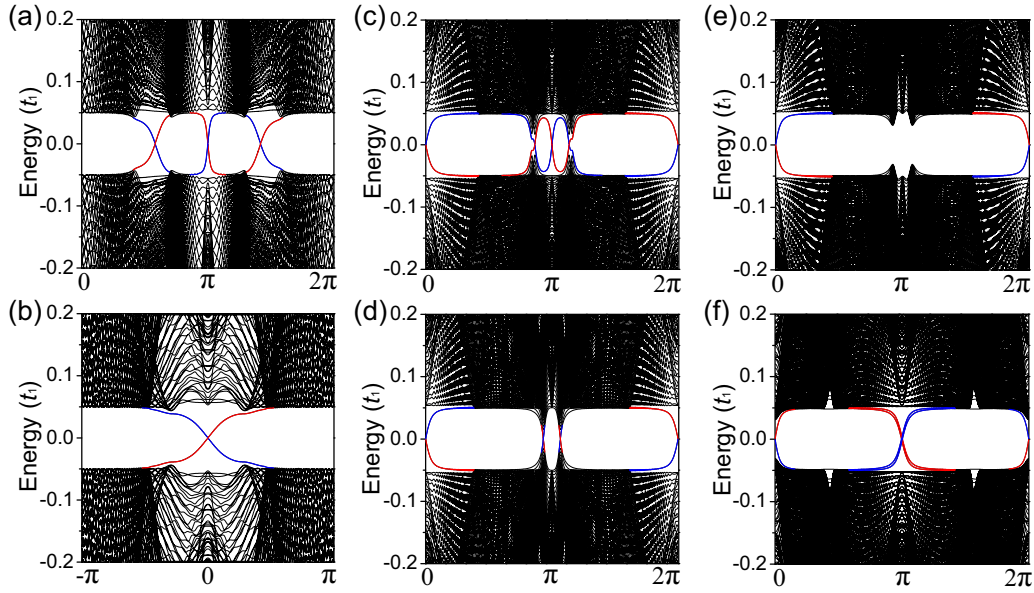
FIG. 4. The chiral MEMs of composited TSC phases from the RNPs (a), (b) at K_c and M_{11}, (c) at K_c and M, and (d)–(f) at M_{11} and M. The red (blue) color represents the MEMs locating at the right (left) edge of the 1D nanoribbon, the periodic direction of which is $a1 + a2$ for (b), (f) and is $a1$ for rest of the figures.

Accordingly, $E(K_c) = E(M)$ can be realized when $\sqrt{2}t_1\lambda_{12} = t_{12}\lambda_1\sqrt{1 - \cos\theta}$, which lead to zero composited Chern number. Despite this, four MEMs emerge at each ribbon edge [Fig. 4(c)], stemming from the RNPs with the Chern number $C = 2$ and -2 for K_c and M points (Table I), respectively. Because the K_c and M points cannot be projected into the same $\mathbf{k}$ point in the BZ of 1D nanoribbon with arbitrary directions, the four MEMs are expected to be robust against the change of edge directions. Moreover, in addition to the hexagonal lattice, one can easily learn the $E(M) = E(M_{11})$ once $t_1 = t_{12}$ [Eqs. (12) and (13)] for centered rectangular lattices, which will induce the total Chern number of -3 (-1) for $\eta < 0$ ($\eta \geqslant 0$). The $C = -3$ TSC phase enables the formation of three MEMs on each edge [Fig. 4(d)], while the MEMs of $C = -1$ phase are dependent on the direction of 1D nanoribbon [Figs. 4(e) and 4(f)]. There is one

MEM on each edge of the ribbon along the (100) direction [Fig. 4(e)], where the M_{11} and M points can be projected to the $\mathbf{k}$ points that are very close with each other in its 1D BZ. This indicates the MEMs will annihilate each other as long as the corresponding RNPs with opposite sign of Chern number are projected to near-$\mathbf{k}$ points, and the ideal case is projected to one $\mathbf{k}$ point exactly [Fig. 4(b)]. Otherwise, multiple MEMs, different from the composited Chern number, will emerge [Figs. 4(a), 4(c), and 4(f)], where the original Chern number of symmetry-enforced equivalent RNPs remains working.

Having demonstrated that the TSC phase can be induced by the RNPs with different ISC, we would like to briefly comment on the comparison between our theoretical models and real materials. Firstly, we only considered single orbital and NN interactions in our generic TB model, which may deviate from the cases when multiple orbitals and long-range interactions exist in real materials. Despite this, we believe our proposed RNPs are complete. The only influence may be that the crystal structures of realizing specific RNPs differ from the corresponding 2D *Bravais* lattices used in TB models (see the next section). Secondly, the assumption of s-wave pairing seems to be oversimplified because the Rashba SOC could induce mixing of the s- and p-wave pairing. Given the intrinsic TSC phase is readily realized when the p-wave component is dominant [60], the TSC phases of different RNPs are expected to be robust against parity mixing of Cooper pairs. Last but not least, the condition of $V_Z^2 > \Delta^2$ for realizing the TSC phases is rather harsh in real materials. Therefore, searching candidate materials that can fulfill this condition appears an important topic in this field. Our work, however, expands the scope of candidate materials by demonstrating that the TSC phases are not limited to a restricted set of materials but in principle can be realized in a wide variety of 2D materials.

TABLE II. The synthesized 2D surface metal layers that could enable ("√") the proposed RNPs.

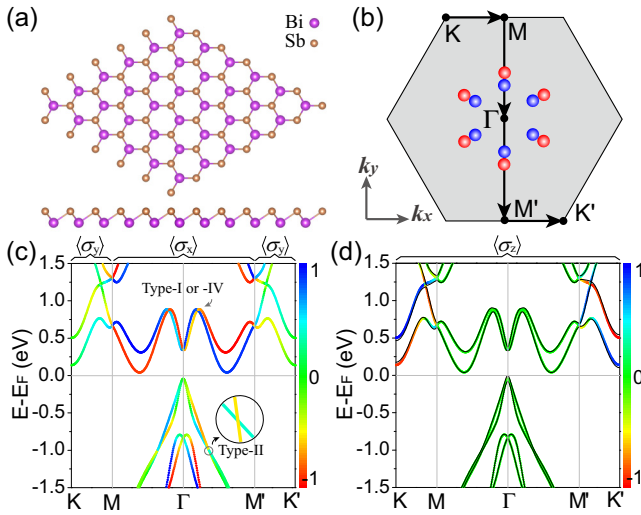| Candidate materials	Type IV	Type III	Type II	Ref.
(Bi,Ag)/Si(111)	√	√	√	[45]
Au/Si(111)$\sqrt{3}\times\sqrt{3}$			√	[46]
(Bi,Na)/Si(111)$\sqrt{3}\times\sqrt{3}$	√			[46]
(Tl,Pb)/Si(111)$\sqrt{3}\times\sqrt{3}$			√	[46–48]
Au/Si(111)5 × 2			√	[49]
In/Si(111)$\sqrt{3}\times\sqrt{7}$	√		√	[50,51]
(Tl,Pb)/Ge(111)$\sqrt{3}\times\sqrt{3}$			√	[47,52]
Pb$_3$Bi/Ge(111)	√		√	[53,54]
Bi/Al$_2$O$_3$(0001)		√		[55]
Pb/Al$_2$O$_3$(0001)		√		[55]
BiPb/Al$_2$O$_3$(0001)		√		[55]
Au/InSe			√	[56]

FIG. 5. (a) Top and side views of BiSb monolayer with the optimized lattice constant of 4.10 Å and the buckling height of 1.74 Å. (b) The high-symmetry paths in the first BZ used for calculating the band structures plotted in (c) and (d). The six blue and six red dots represent the positions of type-I (or -IV) and type-II RNPs, respectively. (c) The band structures with the expectation values of σ_x at the path of M-Γ-M' and of σ_y at K-M (K'-M') paths being represented by colors. Type-I (or -IV) and type-II RNPs deviated from the TRI point are marked in this figure. (d) The band structures with the colors represent the expectation values of σ_z. The black solid lines are the fitted band structures using the WFs, where the out-of-plane directed Zeeman field $V_Z = 40$ meV was introduced.

V. MATERIALS REALIZATION OF THE PROPOSED RNPS WITH EXPECTED TSC

The Rashba SOC widely exists in the 2D materials with the out-of-plane space-inversion symmetry breaking. There are tremendous works reporting the 2D metal layers fabricated on the surface of substrate materials possessing large Rashba spin splitting [45–56]. However, their attentions are mainly focused on the type-I RNPs at TRI points, while other types of RNPs we proposed here are ignored. We searched the reported 2D surface metal layers that could enable the proposed RNPs with the ISC different from $(k_x\sigma_y - k_y\sigma_x)$ in Table II. One can easily conclude the type-IV, type-III, and type-II RNPs

indeed exist in real materials, while the type-I′ one is rare due to the rigorous realizing conditions, e.g., the $t_1 = 2t_{12}$ in our TB model. These RNPs (Table II) are expected to enable the related materials showing TSC. The needed Zeeman gap could be introduced by applying external magnetic field, while the pairing gap can be intrinsic [48,50–52] or induced by the proximity effect.

In addition to the 2D surface metal layers, isolated 2D bulked monolayer also holds the possibility of breaking the space-inversion symmetry, such as the monolayer GeTe [18] and BiSb [61] with honeycomb lattice. We take the BiSb monolayer [Fig. 5(a)] as a represented material to prove the existence of type-I, type-II, and even type-IV RNPs at the **k** points deviated from the TRI points, by using first-principles calculations based on the density-functional theory implemented in the QUANTUM ESPRESSO package [62]. The full relativistic pseudopotential of projector-augmented wave with the functional type of Perdew-Burke-Ernzerhof was employed and the kinetic energy cutoff was set to 60 Ry for wave functions. The BiSb monolayer was simulated by introducing a vacuum region of more than 15 Å, whose lattice constant and atomic positions are fully optimized with considering SOC on the uniform $12 \times 12 \times 1$ **k**-point sampling in BZ.

Following a self-consistent calculation, the electronic band structures are calculated along high-symmetry lines [Fig. 5(b)], as shown in Figs. 5(c) and 5(d). Due to absenting out-of-plane and in-plane inversion symmetry simultaneously, both the Rashba and Ising spin splitting are sparked. The Rashba spin splitting is significant at the **k** points near the center of BZ [Fig. 5(c)], while the Ising one is dominant around the corners of BZ [Fig. 5(d)]. Importantly, one can notice the type-I and -II RNP, respectively, existing in the conduction and valence bands along the path of the Γ-M ($-M'$) direction. Due to the symmetry of honeycomb lattice, there are six type-I and six type-II RNPs in the first BZ [Fig. 5(b)].

To study the TSC of RNPs in BiSb monolayer, we fit the first-principles band structures by employing the WANNIER90-2.1 code [63] under the basis of Wannier functions (WFs), where the p orbitals of Bi and Sb are used as the initial guess for the unitary transformations. This procedure will generate a real-space Hamiltonian, which enables us to construct the momentum space electronic Hamiltonian $h_{\text{WFs}}(\mathbf{k})$ by using Fourier transform. Then the material-specific BdG Hamiltonian can be generally written as

$$h_{\text{WFs}}^{\text{BdG}}(\mathbf{k}) = \begin{pmatrix} h_{\text{WFs}}(\mathbf{k}) + h(V_Z) - E_{\text{RNPs}} & h(\Delta) \\ h^*(\Delta) & -h_{\text{WFs}}^*(-\mathbf{k}) - h(V_Z) + E_{\text{RNPs}} \end{pmatrix}. \tag{22}$$

Here, $h(V_Z)$ denotes the out-of-plane directed Zeeman exchange field and $h(\Delta)$ represents the intraorbitals spin-singlet pairing. Details of this first-principles approach for specific materials have been given previously [18]. With the $h_{\text{WFs}}^{\text{BdG}}(\mathbf{k})$ in hand, we can determine the TSC of specific materials with the RNPs at the energy of E_{RNPs} by calculating the Berry curvature and evaluating the Chern number of pairing gaps.

The dispersion of superconducting quasiparticles with the E_{RNPs} being set to the energy of type-I and -II RNPs in BiSb

monolayer are, respectively, plotted in Figs. S10(a) and S10(c) [58]. We can see a not fully opened but continuous gap exists for type-I RNPs, while the pairing gap associated with type-II RNP is fully opened. The continuous gap is attributed to the interaction between the Ising SOC and the Zeeman field, which leads to unequal eigenvalues between the states at the **k** and the $-\mathbf{k}$ points, as shown by the comparison between the band structures plotted by colored lines and black solid line near the K and K' points in Fig. 5(d). Meanwhile, similar

to our model calculations, the magnitude of the pairing gap varies at different **k** point due to the effect of Pauli paramagnetic mechanism.

The distributions of calculated Berry curvature for the states below the pairing gap condensing at type-I and -II RNPs are, respectively, plotted in Figs. S10(b) and S10(d) [58]. Integrating the Berry curvature leads to the Chern number $C = 6$, due to the existence of six symmetry-equivalent RNPs in the first BZ [Fig. 5(b)]. This indicates the RNPs deviated from TRI points present advantages over the ones at TRI points in inducing high Chern number TSC phases. Moreover, considering strain providing a feasible route to tune the magnitudes of hopping energy and Rashba SOC strength, we anticipate the type-I RNPs in the conduction bands of BiSb monolayer can be transformed to the type-IV and -II RNPs by applying in-plane biaxial strain, based on our TB model prediction. This tendency was already shown by previous report [61]. Because our model calculation indicates this transformation cannot change the TSC phase, the strain-induced type-IV and -II RNP in strained BiSb monolayer are also expected to induce TSC with Chern number $C = 6$. Additionally, preparing the heavy atoms, e.g., Bi, Pb, BiPb, and BiSb monolayer on the surface of $Al_2O_3(0001)$ [55], type-III RNPs emerge, which will definitely enable the TSC phase with Chern number $C = \pm 1$ based on the above analysis.

VI. CONCLUSIONS

By constructing a generic TB model with Rashba SOC on the 2D *Bravais* lattices, we propose the type-IV, -III, -II, and -I$'$ RNPs, whose FS contours and low-energy effective ISC forms are different from that of the known isotropic type-I RNP. Despite this, our calcualtions indicate these proposed RNPs could spark TSC phases with nonzero Chern number and chiral MEMs. High Chern number can be reached for multiple symmetry-equivalent RNPs, especially for the RNPs deviated from TRI points. Moreover, the Chern number can be composited when the symmetry-unequivalent RNPs are equal in energy, where the chiral MEMs are edge dependent. Furthermore, by using first-principles calculations, we demonstrate BiSb monolayer acts as an ideal material platform for realizing the type-I, -II, and even -IV RNPs that are deviated from the TRI point, which give rise to TSC with Chern number $C = 6$. We emphasize these types of RNP widely exist in the 2D materials with the inversion symmetry being broken by buckling or substrates, which not only expands the horizon of finding multiple and edge-dependent MEMs, but also provides promising platforms to investigate physics of Rashba SOC.

[1] E. Majorana, Teoria simmetrica dell'elettrone e del positrone, Nuovo Cimento **14**, 171 (2008).

[2] X.-L. Qi and S.-C. Zhang, Topological insulators and superconductors, Rev. Mod. Phys. **83**, 1057 (2011).

[3] M. Sato and Y. Ando, Topological superconductors: A review, Rep. Prog. Phys. **80**, 076501 (2017).

[4] D. A. Ivanov, Non-Abelian Statistics of Half-Quantum Vortices in *p*-Wave Superconductors, Phys. Rev. Lett. **86**, 268 (2001).

[5] M. Stone and S.-B. Chung, Fusion rules and vortices in $px + ipy$ superconductors, Phys. Rev. B **73**, 014505 (2006).

[6] C. Nayak, S. H. Simon, A. Stern, M. Freedman, and S. Das Sarma, Non-Abelian anyons and topological quantum computation, Rev. Mod. Phys. **80**, 1083 (2008).

[7] A. Y. Kitaev, Fault-tolerant quantum computation by anyons, Ann. Phys. **303**, 2 (2003).

[8] N. Read and D. Green, Paired states of fermions in two dimensions with breaking of parity and time-reversal symmetries and the fractional quantum Hall effect, Phys. Rev. B **61**, 10267 (2000).

[9] A. Y. Kitaev, Unpaired Majorana fermions in quantum wires, Phys.-Usp.+ **44**, 131 (2001).

[10] R. M. Lutchyn, E. P. A. M. Bakkers, L. P. Kouwenhoven, P. Krogstrup, C. M. Marcus, and Y. Oreg, Majorana zero modes in superconductor-semiconductor heterostructures, Nat. Rev. Mater. **3**, 52 (2018).

[11] S. Nadj-Perge, I. K. Drozdov, J. Li, H. Chen, S. Jeon, J. Seo, A. H. MacDonald, B. A. Bernevig, and A. Yazdani, Observation of Majorana fermions in ferromagnetic atomic chains on a superconductor, Science **346**, 602 (2014).

[12] G. C. Ménard, S. Guissart, C. Brun, R. T. Leriche, M. Trif, F. Debontridder, D. Demaille, D. Roditchev, P. l Simon, and T. Cren, Two-dimensional topological superconductivity in Pb/Co/Si(111), Nat. Commun. **8**, 2040 (2017).

[13] S. Kezilebieke, M. N. Huda, V. Vaňo, M. Aapro, S. C. Ganguli, O. J. Silveira, S. Głodzik, A. S. Foster, T. Ojanen, and P. Liljeroth, Topological superconductivity in a van der Waals heterostructure, Nature (London) **588**, 424 (2020).

[14] M. Sato, Y. Takahashi, and S. Fujimoto, Non-Abelian Topological Order in *s*-Wave Superfluids of Ultracold Fermionic Atoms, Phys. Rev. Lett. **103**, 020401 (2009).

[15] R. M. Lutchyn, J. D. Sau, and S. Das Sarma, Majorana Fermions and a Topological Phase Transition in Semiconductor-Superconductor Heterostructures, Phys. Rev. Lett. **105**, 077001 (2010).

[16] Y. Oreg, G. Refael, and F. von Oppen, Helical Liquids and Majorana Bound States in Quantum Wires, Phys. Rev. Lett. **105**, 177002 (2010).

[17] J. D. Sau, R. M. Lutchyn, S. Tewari, and S. Das Sarma, Generic New Platform for Topological Quantum Computation Using Semiconductor Heterostructures, Phys. Rev. Lett. **104**, 040502 (2010).

[18] X. Zhang, K.-H. Jin, J. Mao, M. Zhao, Z. Liu, and F. Liu, Prediction of intrinsic topological superconductivity in Mn-doped

GeTe monolayer from first-principles, npj Comput. Mater. **7**, 44 (2021).

[19] A. A. Soluyanov, D. Gresch, Z. Wang, Q. Wu, M. Troyer, X. Dai, and B. A. Bernevig, Type-II Weyl semimetals, Nature (London) **527**, 495 (2015).

[20] L. Fu and C. L. Kane, Superconducting Proximity Effect and Majorana Fermions at the Surface of a Topological Insulator, Phys. Rev. Lett. **100**, 096407 (2008).

[21] J. Wang, Q. Zhou, B. Lian, and S.-C. Zhang, Chiral topological superconductor and half-integer conductance plateau from quantum anomalous Hall plateau transition, Phys. Rev. B **92**, 064520 (2015).

[22] Q. L. He, L. Pan, A. L. Stern, E. C. Burks, X. Che, G. Yin, J. Wang, B. Lian, Q. Zhou, E. S. Choi *et al.*, Chiral Majorana fermion modes in a quantum anomalous Hall insulator-superconductor structure, Science **357**, 294 (2017).

[23] J.-P. Xu, M.-X. Wang, Z. L. Liu, J.-F. Ge, X. Yang, C. Liu, Z. A. Xu, D. Guan, C. L. Gao, D. Qian *et al.*, Experimental Detection of a Majorana Mode in the core of a Magnetic Vortex inside a Topological Insulator-Superconductor Bi_2Te_3/$NbSe_2$ Heterostructure, Phys. Rev. Lett. **114**, 017001 (2015).

[24] H.-H. Sun, K.-W. Zhang, L.-H. Hu, C. Li, G.-Y. Wang, H.-Y. Ma, Z.-A. Xu, C.-L. Gao, D.-D. Guan, Y.-Y. Li *et al.*, Majorana Zero Mode Detected with Spin Selective Andreev Reflection in the Vortex of a Topological Superconductor, Phys. Rev. Lett. **116**, 257003 (2016).

[25] W. Yu, W. Pan, D. L. Medlin, M. A. Rodriguez, S. R. Lee, Z.-q. Bao, and F. Zhang, π and 4π Josephson Effects Mediated by a Dirac Semimetal, Phys. Rev. Lett. **120**, 177704 (2018).

[26] J. Wiedenmann, E. Bocquillon, R. S. Deacon, S. Hartinger, O. Herrmann, T. M. Klapwijk, L. Maier, C. Ames, C. Brüne, C. Gould, A. Oiwa, K. Ishibashi, S. Tarucha, H. Buhmann, and L. W. Molenkamp, 4π periodic Josephson supercurrent in HgTe-based topological Josephson junctions, Nat. Commun. **7**, 10303 (2016).

[27] X.-P. Li, K. Deng, B. Fu, Y. K. Li, D.-S. Ma, J. F. Han, J. Zhou, S. Zhou, and Y. Yao, Type-III Weyl semimetals: $(TaSe_4)_2$I, Phys. Rev. B **103**, L081402 (2021).

[28] L. Jin, X. Zhang, Y. Liu, X. Dai, L. Wang, and G. Liu, Fully spin-polarized double-Weyl fermions with type-III dispersion in the quasi-one-dimensional materials X_2RhF_6 (X=K, Rb, Cs), Phys. Rev. B **102**, 195104 (2020).

[29] A. P. Schnyder, S. Ryu, A. Furusaki, and A. W. W. Ludwig, Classification of topological insulators and superconductors in three spatial dimensions, Phys. Rev. B **78**, 195125 (2008).

[30] S. Rachel, E. Mascot, S. Cocklin, M. Vojta, and D. K. Morr, Quantized charge transport in chiral Majorana edge modes, Phys. Rev. B **96**, 205131 (2017).

[31] M. Banerjee, M. Heiblum, V. Umansky, D. E. Feldman, Y. Oreg, and A. Stern, Observation of half-integer thermal Hall conductance, Nature (London) **559**, 205 (2018).

[32] Y. Kasahara, T. Ohnishi, Y. Mizukami, O. Tanaka, S. Ma, K. Sugii, N. Kurita, H. Tanaka, J. Nasu, Y. Motome, T. Shibauchi, and Y. Matsuda, Majorana quantization and half-integer thermal quantum Hall effect in a Kitaev spin liquid, Nature (London) **559**, 227 (2018).

[33] B. Lian, X.-Q. Sun, A. Vaezi, X.-L. Qi, and S.-C. Zhang, Topological quantum computation based on chiral Majorana fermions, Proc. Natl. Acad. Sci. U.S.A. **115**, 10938 (2018).

[34] C. W. J. Beenakker, P. Baireuther, Y. Herasymenko, I. Adagideli, L. Wang, and A. R. Akhmerov, Deterministic Creation and Braiding of Chiral Edge Vortices, Phys. Rev. Lett. **122**, 146803 (2019).

[35] X.-L. Qi, T. L. Hughes, and S.-C. Zhang, Chiral topological superconductor from the quantum Hall state, Phys. Rev. B **82**, 184516 (2010).

[36] Y.-T. Hsu, A. Vaezi, M. H. Fischer, and E.-A. Kim, Topological superconductivity in monolayer transition metal dichalcogenides, Nat. Commun. **8**, 14985 (2017).

[37] X.-P. Liu, Y. Zhou, Y.-F. Wang, and C.-D. Gong, Characterizations of topological superconductors: Chern numbers, edge states and Majorana zero modes, New J. Phys. **19**, 093018 (2017).

[38] X. Zhang and F. Liu, Prediction of Majorana edge states from magnetized topological surface states, Phys. Rev. B **103**, 024405 (2021).

[39] O. Can, T. Tummuru, R. P. Day, I. Elfimov, A. Damascelli, and M. Franz, High-temperature topological superconductivity in twisted double-layer copper oxides, Nat. Phys. **17**, 519 (2021).

[40] J. Röntynen and T. Ojanen, Topological Superconductivity and High Chern Numbers in 2D Ferromagnetic Shiba Lattices, Phys. Rev. Lett. **114**, 236803 (2015).

[41] J. Li, T. Neupert, Z. Wang, A. H. MacDonald, A. Yazdani, and B. A. Bernevig, Two-dimensional chiral topological superconductivity in Shiba lattices, Nat. Commun. **7**, 12297 (2016).

[42] L. Wang and M. W. Wu, Topological superconductor with a large Chern number and a large bulk excitation gap in single-layer graphene, Phys. Rev. B **93**, 054502 (2016).

[43] J. Röntynen and T. Ojanen, Chern mosaic: Topology of chiral superconductivity on ferromagnetic adatom lattices, Phys. Rev. B **93**, 094521 (2016).

[44] S. Sun, W. Qin, L. Li, and Z. Zhang, Chiral topological superconducting state with Chern number $C = -2$ in Pb_3Bi/$Ge(111)$, Phys. Rev. B **103**, 235149 (2021).

[45] N. V. Denisov, E. N. Chukurov, Y. V. Luniakov, O. A. Utas, S. G. Azatyan, A. A. Yakovlev, A. V. Zotov, and A. A. Saranin, Two-dimensional bismuth–silver structures on Si(111), Surf. Sci. **623**, 17 (2014).

[46] D. V. Gruznev, A. V. Zotov, and A. A. Saranin, Tailoring of spin-split metallic surface-state bands on silicon, J. Electron Spectrosc. **201**, 81 (2015).

[47] D. V. Gruznev, L. V. Bondarenko, A. Y. Tupchaya, S. V. Eremeev, A. N. Mihalyuk, J. P. Chou, C. M. Wei, A. V. Zotov, and A. A. Saranin, 2D Tl-Pb compounds on Ge(111) surface: Atomic arrangement and electronic band structure, J. Phys. **29**, 035001 (2016).

[48] A. V. Matetskiy, S. Ichinokura, L. V. Bondarenko, A. Y. Tupchaya, D. V. Gruznev, A. V. Zotov, A. A. Saranin, R. Hobara, A. Takayama, and S. Hasegawa, Two-Dimensional Superconductor with a Giant Rashba Effect: One-Atom-Layer Tl-Pb Compound on Si(111), Phys. Rev. Lett. **115**, 147003 (2015).

[49] K. Taguchi, K. Sumida, Y. Okuda, K. Miyamoto, A. Kimura, T. Oguchi, and T. Okuda, Spectroscopic evidence of quasi-one-dimensional metallic Rashba spin-split states on the Si(111)5 × 2-Au surface, Phys. Rev. B **101**, 045430 (2020).

[50] S. Yoshizawa, T. Kobayashi, Y. Nakata, K. Yaji, K. Yokota, F. Komori, S. Shin, K. Sakamoto, and T. Uchihashi, Atomic-

layer Rashba-type superconductor protected by dynamic spin-momentum locking, Nat. Commun. **12**, 1462 (2021).

[51] T. Zhang, P. Cheng, W.-J. Li, Y.-J. Sun, G. Wang, X.-G. Zhu, K. He, L. Wang, X. Ma, X. Chen *et al.*, Superconductivity in one-atomic-layer metal films grown on Si(111), Nat. Phys. **6**, 104 (2010).

[52] T. Nakamura, A. Takayama, R. Hobara, D. V. Gruznev, A. V. Zotov, A. A. Saranin, and S. Hasegawa, Superconducting single-atomic-layer Tl-Pb compounds on Ge(111) and Si(111) surfaces, Appl. Surf. Sci. **479**, 679 (2019).

[53] L. Li, S. Ren, W. Qin, S. Zhang, X. Wan, Y. Jia, P. Cui, and Z. Zhang, Emergence of Van Hove singularity and topological states in Pb_3Bi/Ge(111) Rashba systems, Phys. Rev. B **102**, 035150 (2020).

[54] W. Qin, L. Li, and Z. Zhang, Chiral topological superconductivity arising from the interplay of geometric phase and electron correlation, Nat. Phys. **15**, 796 (2019).

[55] M. Chen and F. Liu, Prediction of giant and ideal Rashba-type splitting in ordered alloy monolayers grown on a polar surface, Nat. Sci. Rev. **8**, nwaa241 (2021).

[56] W. Ming, Z. F. Wang, M. Zhou, M. Yoon, and F. Liu, Formation of ideal Rashba states on layered semiconductor surfaces steered by strain engineering, Nano Lett. **16**, 404 (2016).

[57] C. Lei, H. Chen, and A. H. MacDonald, Ultrathin Films of Superconducting Metals as a Platform for Topological Superconductivity, Phys. Rev. Lett. **121**, 227701 (2018).

[58] See Supplemental Material at http://link.aps.org/supplemental/10.1103/PhysRevB.104.245409 for supplemental figures.

[59] W.-Y. He, B. T. Zhou, J. J. He, N. F. Q. Yuan, T. Zhang, and K. T. Law, Magnetic field driven nodal topological superconductivity in monolayer transition metal dichalcogenides, Commun. Phys. **1**, 40 (2018).

[60] M. Sato and S. Fujimoto, Topological phases of noncentrosymmetric superconductors: Edge states, Majorana fermions, and non-Abelian statistics, Phys. Rev. B **79**, 094504 (2009).

[61] S. Singh and A. H. Romero, Giant tunable Rashba spin splitting in a two-dimensional BiSb monolayer and in BiSb/AlN heterostructures, Phys. Rev. B **95**, 165444 (2017).

[62] G. Paolo, B. Stefano, B. Nicola, C. Matteo, C. Roberto, C. Carlo, C. Davide, C. Guido, C. Matteo, D. Ismaila *et al.*, QUANTUM ESPRESSO: A modular and open-source software project for quantum simulations of materials, J. Phys. **21**, 395502 (2009).

[63] A. A. Mostofi, J. R. Yates, G. Pizzi, Y.-S. Lee, I. Souza, D. Vanderbilt, and N. Marzari, An updated version of wannier90: A tool for obtaining maximally-localised Wannier functions, Comput. Phys. Commun. **185**, 2309 (2014).